Simulation study of a pulsed DBD with an electrode containing charge injector parts

N. Pourali[a*], M. M. Sarafraz[a,b], V. Hessel[a,b] E.V. Rebrov[a,c,d]

[a]*School of Engineering, University of Warwick, Coventry CV4 7AL, United Kingdom.*

[b]*School of Chemical Engineering and Advanced Materials,*

the University of Adelaide, Adelaide 5005, South Australia, Australia.

[c]*Department of Chemical Engineering and Chemistry,*

Eindhoven University of Technology, P.O. Box 513,

5600 MB Eindhoven, The Netherlands. and

[d]*St. Petersburg State Institute Technology (Technical University),*

Moskovsky pr. 26, 190013, St. Petersburg, Russia.

Abstract

By using a multi-species fluid model the tunability and controllability of plasma parameters such as distributions of electron density, electron energy, ion density, and electric field in a micro-DBD with charge injector electrode and driven by negatively polarized nanosecond pulsed voltage superimposed on a positive dc bias voltage are investigated. To this end, the effects of changing features of pulsed voltage like pulse rise time (10-20 ns), pulse peak width (10-15 ns), and pulse fall time (20-30 ns) on characteristics of argon plasma formed inside the reactor are studied. The results show that with the increase of pulse width and pulse rise time, the density of electron and ion increase while fall time change does not significantly affect the plasma parameters. Generally, the results of this study explicitly prove the possibility of controlling plasma formed inside DBD reactors driven by negative pulse voltage combined with a positive DC voltage, which is very important in waste gas conversion applications.

* Corresponding author: n.pourali86@gmail.com , Nima.Pourali@warwick.ac.uk

I. INTRODUCTION

Non-thermal plasmas, also known as non-equilibrium plasmas, that contain energetic electrons with temperature 1-15eV and ions and neutral species (radicals, excited atom and molecules, background gases) having temperature of order few hundreds Kelvin has recently found numerous applications in different fields such as biomedicine [1, 2], sterilization [3, 4], organic chemistry [5], environmental pollution treatment [6, 7], flow control [8], triboelectric [9], nano-generators [10], cell fuels [11], and ignition combustion [12]. There are a lot of procedures and sources to generate non-thermal plasmas, but only a few of them such as corona discharge, high energy electron beam, and dielectric barrier discharge can produce this kind of plasmas in the atmospheric pressure range, which are employed in environmental applications. Among these, dielectric barrier discharge (DBD) in comparison to the other systems is known by its considerably high specific power density, strong potential for upscaling, and low gas consumption. Consequently, atmospheric pressure DBD with the capability to generate energetic electrons to overcome thermodynamic obstacles have been a good candidate to be applied for remediation of gaseous waste streams and the destruction of volatile organic compounds (VOCs) and also a great deal of effort in recent years has been devoted to using the DBD in other applications such as surface treatments, high-power lasers, excimer UV light sources, and plasma display panels.

In its common configuration, a dielectric barrier discharge consists of two electrodes that are separated by one or more dielectric layer and a discharge gap [13]. The dielectric barrier is inserted to prevent the plasma transition to arc or spark regime (very common in high-voltage corona discharges) and maintaining the temperature of heavy species being low [14]. Depending on the structure of electrodes, dielectric surface properties, characteristics of operating power, the gas mixer, and gas pressure and temperature, the DBD can show diffuse or glow and filamentary modes [15, 16]. The diffuse or glow mode is uniform, stable and homogeneous environment and temporal features inside it are stable and reproducible. This mode usually appears at low pressure operating conditions and pure single background gas, so it is favored in the semiconductor industry for plasma etching and plasma deposition processes. On the other hand, in atmospheric and higher pressure ranges, most of DBD configurations operate in the filamentary regime and electrical breakdown in a large number of micro discharges is the normal situation for them. Spatially non-uniform streamers and tiny short-lived current filaments are called micro-discharges. Therefore, the main focus of fundamental research on the environmental application of atmospheric

pressure DBD is recently devoted to tailoring micro discharge features by adjusting temperature and pressure, using the electrodes with special shapes and geometry, and dielectric barriers with specific properties. The most important reason for this is that the radius of a propagating streamer can be affected by these parameters and by gas density.

As mentioned before, the atmospheric DBD plasmas have a high tendency to instabilities and they are non-uniform and inhomogeneous. A more favorable way to tackle this problem is to decrease the discharge gap of the DBD reactor and confining the plasma to dimensions less than 1 mm [17]. In this way having atmospheric-pressure plasma operating in glow or diffuse regime becomes feasible and desired uniformity and stability can be achieved. This kind of weakly ionized plasmas that are referred to as micro-plasmas or microreactors can promote the efficient production of transient molecular species and they are also capable to offer better control of processing parameters for selective synthesis of particular products [18, 19].

It could be claimed that among plasma reactors powered with different voltage sources, pulsed plasma generators have shown better results for the destruction of volatile organic compounds and flue gas decomposition [20–25]. They initiate discontinuous discharge that prevents remarkable heat losses between pulses and improves the energy efficiency and the discharge stability without overheating effect. As a result, a high nonequilibrium discharge is achievable with smaller total discharge power. Also, in the sub-microsecond time scale, they result in significant shifts in the distribution functions of temperatures and energies associated with the ions and electrons. This allows for the selective production of chemically reactive species and opens the door to a wide range of new applications of microplasmas. Besides, in microplasma powered by pulsed generators, the charge efficiency can be enhanced by shortening pulse rise time and width to the micro or nanosecond scale. Consequently, narrower pulse width (i.e., micro or nanosecond scale) is in favor of breaking bonds of feed molecules rather than heating the gas bulk and surrounding materials.

Depending on the polarity of the voltage applied to a DBD reactor, self-sustainability of plasma formed by that can change. The higher self-sustainability occurs by a negative applied voltage [26]. When the discharge gap in a direct-current plasma reactor is bigger than 10 μm the field emission effects are negligible and the most important factor of self-sustainability becomes the intensity of secondary electron emission from electrodes and reactor walls [27, 28]. The secondary electron emission appears when plasma ions are accelerated under the affection of the electric field of plasma sheath formed on walls and electrodes and collide with them energetically to release the electron. The flux of secondary electron emission is proportional to the velocity of ions, which

is directly dependent on the electric field intensity. It is obvious that when the potential of an electrode is highly negative the possibility of secondary electron emission rises due to the increase in the intensity of interaction of the electric field and the positive ions. Also, in sharp point where there is an accumulation of the electric field, again, the secondary emission process can be more intensive due to the high intensity of the electric field. These sharp points are defined as charge injection parts.

Our precise review of the literature reveals that although surface dielectric barrier plasma actuators driven by pulsed voltage supply have been studied a lot, in the electro-hydrodynamic field in order to air flow control, there is no report considering effects of characteristics of nanosecond pulsed power upon the behavior of plasma formed inside the micro-DBD reactors used in gas conversion applications. As, in the simulation of these plasma reactors only ac voltage sources have been used as power supply [29, 30]. Therefore, by following outline of our multi-disciplinary international project, European Research Council Synergy Grant SCOPE 810182, which deals with the synergy between catalytic materials and fast-modulated micro-plasma array in order to increase the energy efficiency and yield of waste gas conversion, in this work, we tend to study the behavior of argon plasma formed in a micro-DBD with one electrode containing charge injection points and driven by nanosecond pulsed voltage in order to obtain an in-depth understanding from the physics of the system and to check how pulse shape can affect the plasma parameters. To this end, a multi-species fluid model that combines transport and momentum equations for each species as well as energy balance relations with the Poisson equation to anticipate the behavior of the system will be used. In the next section, the structure of the reactor and the employed model will be described while section III presents and discusses the results of the simulation. Finally, section IV is devoted to the conclusion and summarizing the main findings.

II. DESCRIPTION OF THE MODEL AND STRUCTURE

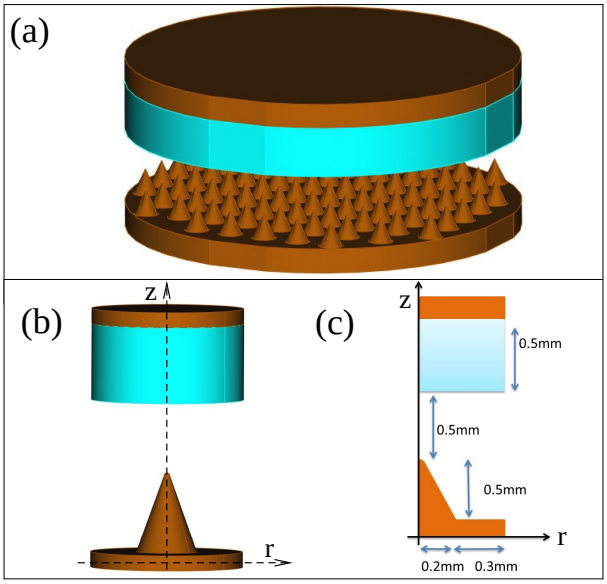

FIG. 1: (a) Complete structure of the DBD reactor, (b) 3D unit cell of the reactor (c) axisymmetric 2D computational domain.

The structure of the plasma reactor considered in this work is displayed in Fig. 1(a). It consists of two electrodes (grounded and powered) and a PET (Polyethylene terephthalate) dielectric barrier layer that covers the upper electrode (grounded electrode). The bottom electrode (powered) is engraved to a periodic cone-shape sharp array, establishing charge injection phenomena. The dielectric layer has a thickness equal with 0.5 mm and the distance between the tip of cones and surface of the dielectric layer is 0.5 mm. The radius of the circular cone base is selected to be 0.2 mm and the height of cones and septation distance between them are fixed to 0.5 mm and 1 mm, respectively. Also, since in reality, there is not an infinite sharp point the curvature radius of the cone tip was selected to be 25 μm. For this structure, the length of the discharge gap is $d = 0.5$ mm and the mean free path, based on the momentum transfer collision frequency of electrons and neutrals, at pressure 1 atm and background gas temperature 300 K is $\lambda \simeq$100 nm. With these conditions, the Knudsen number ($Kn = \lambda/d$) comparing the geometric length scale with the mean free path of the collisions is very small ($\simeq 2 \times 10^{-4}$), implying that non-continuum effects are negligible. Therefore, using the kinetic or hybrid models which need a high run-time cost is not essential and a fluid approach could be sufficient to replicate the real system and provide a correct thorough understanding of the discharge behavior. The 3-D modeling of the whole

system is very complex. However, with bearing in mind the periodicity of system, a 2D axisymmetric fluid modeling of a periodic unit (Fig.1 (c)) will also be able to mimic the actual problem. The fluid approach used here is based on solving a set of coupled differential equations that express the conservation of mass, momentum, and energy, for the different plasma species. This approach has widely been used in previous simulation studies related to DBD devices such as DBD gas discharges in gas conversion applications in plasma chemistry area [30–32] and surface DBD actuators in air flow control applications in elctrohydrodynamics field [33–35]. The mass conservation equation is given as:

$$\frac{\partial n_j}{\partial t} + \overrightarrow{\nabla}.\overrightarrow{\Gamma}_j = \omega_j, \tag{1}$$

where n_j is density of species $j = i, e, n$ (ion, electron and neutral, respectively), $\overrightarrow{\Gamma}_j$ stands for flux and ω_j refers to species source term. The fluxes are calculated by the drift-diffusion approximation as:

$$\overrightarrow{\Gamma_j} = -D_j \overrightarrow{\nabla} n_j \pm \mu_j \overrightarrow{E} n_j, \tag{2}$$

where the first term on the right-hand side describes the diffusion while the second term determines the electric drift which is zero for neutrals. D_j and μ_j are the diffusion and mobility coefficients of the species j, respectively, and $\overrightarrow{E}$ is the electric field with the signs plus and minus for ions and electrons, respectively. The source term ω_j in equation (1) is obtained by considering the volume reactions in which species are created or lost as bellow:

$$\omega_j = \sum_k [(a_{jk}^R - a_{jk}^L) k_k \prod_l n_l^L], \tag{3}$$

where a_{jk}^R and a_{jk}^L are the right-hand side and left-hand side stoichiometric coefficients of species j in reaction k , k_k is the reaction rate coefficient and n_l^L is the density of the *l*-th species in the left-hand side of reaction k. The energy balance equations for ions and neutrals are disregarded in this model and it is assumed that ions have the same temperature of background gas and are constants throughout the reactors. Therefore, here, the energy balance equation will be solved only for the electrons, which is expressed as:

$$\frac{\partial n_\varepsilon}{\partial t} + \overrightarrow{\nabla}.\overrightarrow{\Gamma}_\varepsilon + \overrightarrow{\Gamma}_e.\overrightarrow{E} = S_\varepsilon, \tag{4}$$

where n_ε is the electron energy density, S_ε is the energy loss/gain due to collisions, and the flux vector for electron energy $\vec{\Gamma}_\varepsilon$ is given as

$$\overrightarrow{\Gamma_\varepsilon} = -\tfrac{5}{3}\mu_e \overrightarrow{E} n_\varepsilon - \tfrac{5}{3} D_e \overrightarrow{\nabla} n_\varepsilon, \tag{5}$$

The set of fluid equations is completed with Poisson equation for electric potential:

$$\vec{\nabla}.(\varepsilon_r \varepsilon_0 \vec{E}) = -\vec{\nabla}.(\varepsilon_r \varepsilon_0 \vec{\nabla} V) = e(\sum_i n_i - n_e), \tag{6}$$

ε_0 is the permittivity of vacuum, ε_r the relative permittivity of the material or the gas, V is the potential and e is the elementary charge. Notice that, unlike the discharge gap region, in the dielectric area the transport and energy equations are not considered and only the Poisson equation with zero space charge density (Laplace equation) is solved for the electric potential. The solution of the Laplace equation in the dielectric region and solution of the Poisson equation in the plasma region are connected self consistently to each other by boundary condition considered at the interface between two media. As a converged solution for potential distribution in the whole domain is obtained when potential continuity in interface boundary is established by applying the following boundary condition:

$$\varepsilon_{diel} \vec{E}_{diel}.\vec{n} - \vec{E}_{gas}.\vec{n} = \sigma/\varepsilon_0 \tag{7}$$

where ε_{diel} is dielectric constant of the insulating layer (PET) that is fixed to 3.4, $\vec{n}$ is the unit normal, and $\vec{E}_{diel}$ and $\vec{E}_{gas}$ are the electric fields in dielectric and discharge sides of the boundary. Surface charge accumulation on the dielectric layer, σ, due to difference in fluxes between the electrons and ions is calculated by:

$$\frac{\partial \sigma}{\partial t} = \overrightarrow{n}.\overrightarrow{J}_i - \overrightarrow{n}.\overrightarrow{J}_e, \tag{8}$$

where $\overrightarrow{J}_i$ and $\overrightarrow{J}_e$ are the total ion and electron current densities at the wall, which are determined by species flux ($\vec{J}_j = q_j \vec{\Gamma}_j$).

The chemistry of argon plasma considered here is the same as the reference [36]. Five species (e, Ar, Ar^*, Ar_2^+, Ar^+) are considered in the chemistry mechanism. These five species participate in 12 reactions to form a complete and closed reactions mechanism (see table II of reference [36]). The reaction rates of reactions occurring between heavy species have been presented there, but for reactions that electron incorporates in them, we use Boltzmann equation solver, BOLSIG+ [37],

to form look-up tables which give electron reactions rates for each mean electron energy value. The transport coefficient of ions and neutral species are extracted from the table I of this reference. The electron mobility and diffusion coefficients are also calculated from the Boltzmann solver and are sorted as a function of the electron mean energy in the look-up tables. In each time step, the local electron reaction rates and electron transport coefficient have been interpolated from look-up tables. The upper electrode was grounded while the bottom electrode is powered by a voltage waveform combined of a repetitive negative nanosecond pulses and a positive dc bias (see Fig. 2). As the figure shows, a single pulse consists of three parts such as pulse rise time (t_r=10 ns), pulse peak width (t_p=10 ns), and pulse fall time (t_f=20 ns). The positive bias voltage is fixed in 400 V and repetition frequency of pulsed voltage is assumed to be constant in 10 kHz [33–35, 38].

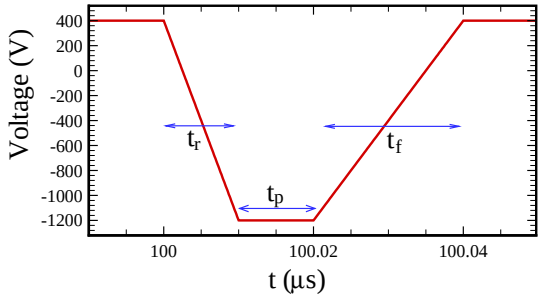

FIG. 2: Shape of nanosecond pulse of -1600 V amplitude with repetition rate of 10 kHz, rise time of t_r =10 ns, pulse peak width of t_p =10 ns and fall time of t_f =20 ns superimposed on a dc bias of 400 V.

In the lateral side of the computational cell, the periodic condition must be applied. To this end, we need to consider that in this boundary, two adjacent unit cells create the same electric field and species fluxes but in opposite direction. Therefore, the normal component of electric fields and normal fluxes of species for two adjacent cells balance each other. This results in zero value for the net normal electric field and normal fluxes of species in the boundary. Therefore, we must set the normal fluxes of electrons and electron energy on this boundary to zero, and assume a zero charge boundary condition, defining the normal electric displacement equal to zero. It is obvious that when the normal electric field is zero forcing the normal component of flux in the left-hand side of Eq.(2) to zero leads to that the normal gradient of species across the boundary becomes zero. The combination of these boundary conditions provides periodicity, which has also been explained previously in reference [39]. The other boundary conditions, considered surface reactions and the parameters of secondary electron emission are as same as those of reference [36].

The field emission effects are not considered because these effects appear at size lengths smaller than 10 μm [40].

III. SIMULATION RESULTS AND DISCUSSION

This section presents the results of the simulation of the structure presented in previous section for gas temperature and total pressure fixed respectively to 300 K and 1 atm. The simulation was done in the COMSOL software which is based on the finite element method. A non-uniform mesh was applied to the domain. It was dense near the cone tip and the dielectric layer surface and become coarser in other regions. It is noteworthy to mention that in the plasma the typical thickness of the space charge region near electrodes and walls is a few electron Debye lengths. The later for the plasma in the gas discharge condition lies in the range $10^{-5}m - 10^{-4}m$. Therefore, to take space charge effect and plasma sheath formation into account mesh size near the electrodes and walls must be smaller than electron Debye lengths. Also, mesh size near the sharp points must be smaller than their curvature radius in order to see charge injection effects. Therefore, a mesh size as small as $2\mu m$ was chosen near the cone tip and near the dielectric layer surface. Also, automatic adaptive mesh refinement as an option in the COMSOL study setting was activated to achieve reliable results. The relative tolerance, which is the convergence criteria value and is defined as $\mid (X_{new} - X_{old})/X_{new} \mid$ (X being the value of calculated parameters), was selected to be 0.0001. This value is 10 times smaller than the default value provided by the COMSOL study setting. It was selected in a such way that the result of simulation did not change for values smaller than it. In order to achieve reliable results, the time step in a time-dependent solver must be selected in such a way that any instant time-dependent change is taken into account. During pulse on time, the smallest time interval is 10 ns that is assumed for the pulse rise time. It requires that this interval must be divided at least to 100 time-points in order to capture the effects of voltage change in the interval and at interval ends. With bearing this in mind, for each time interval, value of time step is chosen in a such way that for values smaller than it the results are unchanged. The time steps during the pulse on-time were shorter than 0.01 ns while during the pulse off-time it was bigger than 1 ns.

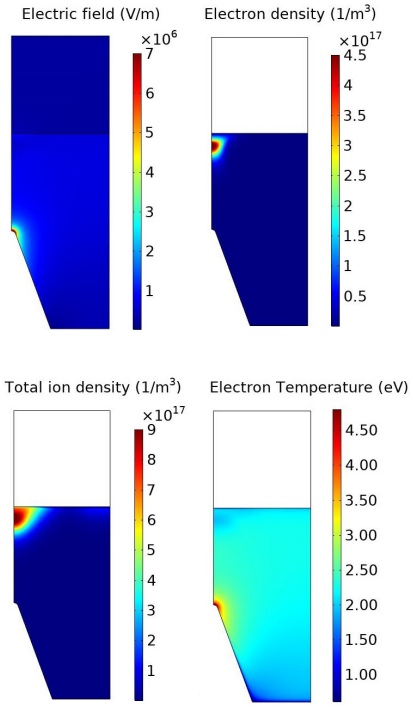

FIG. 3: The spatial distributions for time-averaged on a single pulse of different plasma parameters: the electron density, total ion density, the electron temperature, and the electric field.

Figure 3 shows the time-averaged distribution of electron density, total ion density, electric field, and electron temperature on a single pulse voltage shown in Fig. 2. Here and hereinafter every "ion" word briefly points out to total ion ($Ar_2^+ + Ar^+$). The total pulse duration is 40 ns. As can be seen from the figure, the peaks of averaged electric field and averaged electron temperature appear in the cone tip region while the density of electron and ion get their maximum value near the dielectric layer surface. It can also be seen that the maximum value of electron density is smaller than that of ion density and it is more localized. The electron density peak location, compared with ion peak location, is positioned further away from the dielectric layer, which is the result of surface charge accumulation on the dielectric layer surface.

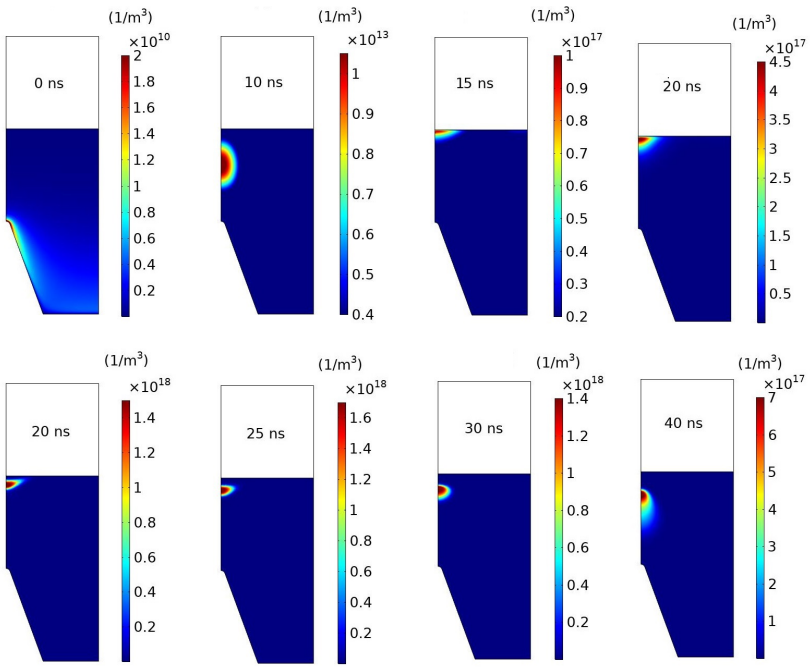

FIG. 4: Time evolution of electron density distribution during pulse on-time.

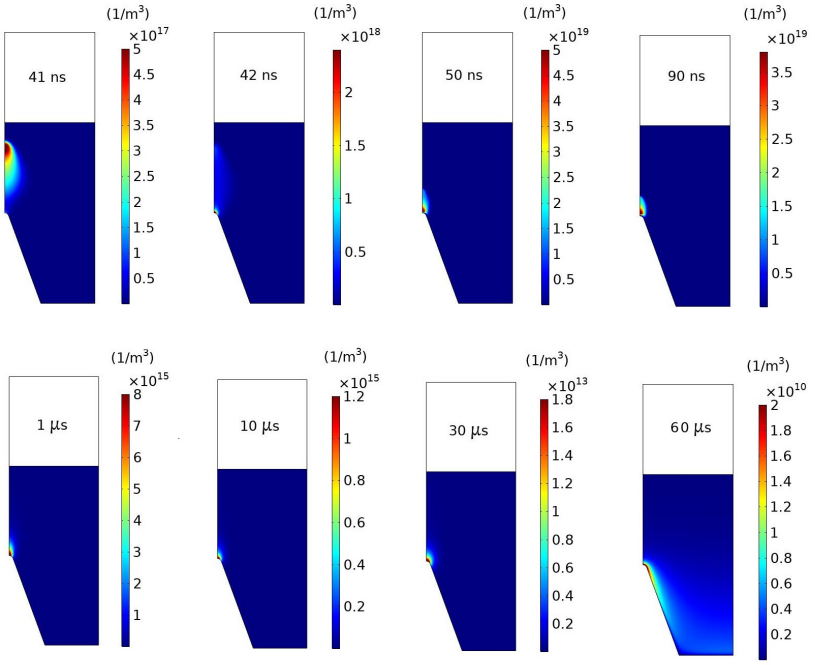

FIG. 5: Time evolution of electron density distribution during pulse off-time.

To a more detailed investigation of the behavior of discharge, the electron density distribution

at different times during pulse on-time is displayed in Fig. 4. The snapshot at t=0 represents the electron density created only with biased voltage +400 V, after this time the negative nanosecond pulse voltage is started. Through increase in the pulsed voltage, the electron avalanche begins to move from the cone tip towards the dielectric layer. During the movement, it becomes more localized and its value increases. This process continues until t=20 ns when pulse fall starts. During the pulse fall time, the electron avalanche comes back from the dielectric layer towards the electrode. In the initial time of the pulse fall interval, the density of electron first increases but with more decrease of net applied voltage after t=35 ns it is going to decrease. At the end of the pulse fall interval, the electrons in front of the avalanche show a tendency to jump towards the electrode and it seems there will be a transition after pulse-off time. This requires that the behavior of discharge after pulse on-time should be investigated. Therefore, in figure 5 we present the snapshots of electron density at several times between 40 ns to 60 μs. As can be seen from the first two snapshots, after pulse switching-off, the electrons are accelerated by the electric field of the positive bias voltage of the electrode and they move very quickly to reach the cone tip during a time of 3 ns. The accumulation of electrons near the cone tip continues until the electric field of positive bias voltages covered by sheath formation around it and the electrons are pushed back by sheath electric field, which occurs at t= 90 ns. After this moment, the electron density starts to decrease very slowly, and finally, at t= 60 μs it reaches its initial value observed at the start of the pulse (t=0 at Fig. 4). It is noteworthy to mention that for a frequency of 10 kHz, the time septation between pulses (100 μs) is bigger than t=60 μs. Therefore, there is no overlap between different pulse effects and during the pulse off-time the plasma has enough time to restore its initial value resulted from just the positive bias voltage, before the next pulse starts.

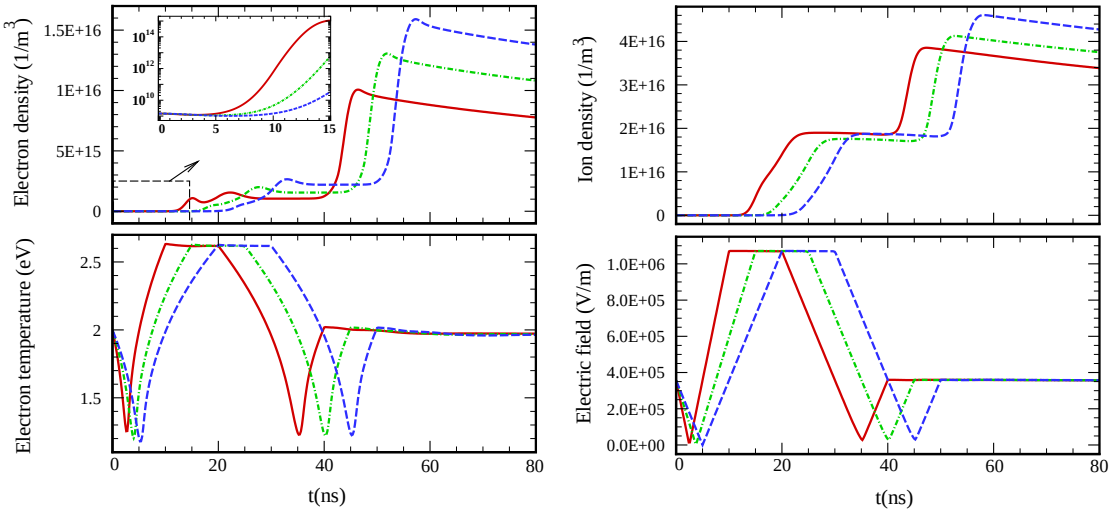

FIG. 6: Spatially averaged electron density, ion density, electron temperature, and electric field as the functions of time for three different pulse rise times 10 ns (solid), 15 ns (dash-dotted), and 20 ns (dashed).

To investigate the effect of the shape of nanosecond pulse voltage on characteristics of plasma, firstly, the pulse rise time is considered as a variable. Therefore, figure 6 compares the time evolution of the spatially averaged density of charged plasma species (ion and electron) as well as electric field and electron energy for three different pulse shapes that have different pulse rise times. Each pulse has the same pulse peak width 10 ns and pulse fall time 20 ns while three different pulse rise times are 10 ns, 15 ns, 20 ns. According to the figure, for all three pulses, the most significant increase in electron density occur just 5 ns after pulse duration time i.e t=45 ns for the pulse with the rise time 10 ns, t=50 ns for the pulse with the rise time 15 ns, and t=55 ns for the pulse with the rise time 20 ns. While the ion density experiences two remarkable increases in value: one during pulse the peak time interval and another (like the electron density) after the pulse on-time. Both the electron density and the ion density stagnate during pulse fall time. After reaching their maximum values, the densities of electron and ion start to decrease slowly during the pulse-off time, as explained previously. Regarding electric field and electron energy, two dips appeared in time evolution of electric field and electron energy profiles, each one is related to one of the moments when the net applied voltage is zero. By comparing the figures it can be found out that increase in pulse rise time results in an increase in both electron density and ion density. The electron temperature and electric field do not experience an increase in their value and only the dip time points for them occur later.

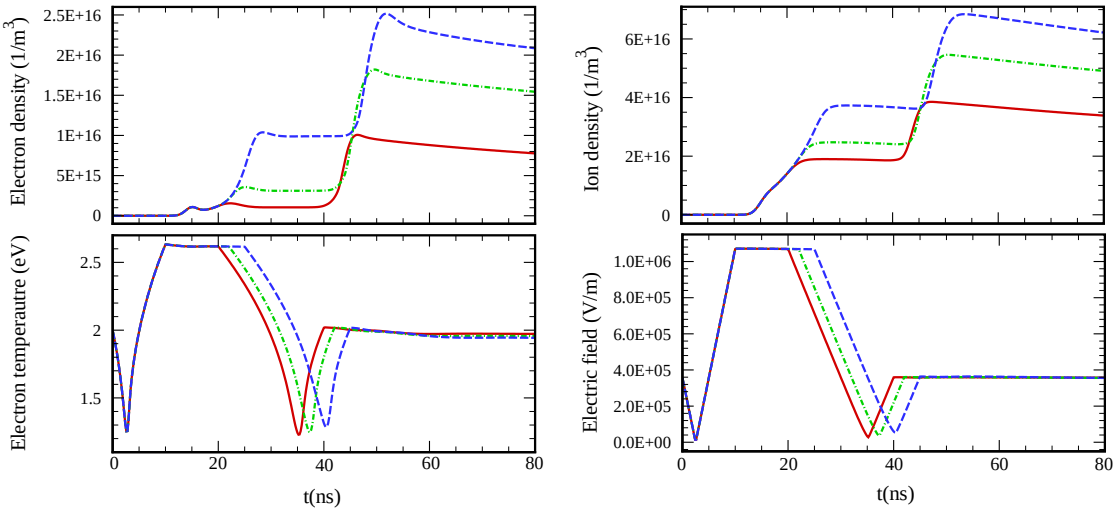

FIG. 7: Spatially averaged electron density, ion density, electron temperature, and electric field as functions of time for three different pulse peak width values 10 ns (solid), 12 ns (dash-dotted), and 15 ns (dashed).

Our main aim to present Fig. 7 is to study the effects of change in pulse width on plasma parameters. Therefore, this figure shows the plasma characteristics for three applied pulses with different pulse peak widths and same pulse rise and fall times. The figure reveal that increase in pulse peak width increases both the electron density and ion density, but that is more vigorous for electron density. It also leads to that electron density and ion density profiles become more similar to each other (compare the electron density and ion density profiles for the pulse with peak width 15 ns). In addition, by comparing the electron density profiles with each other it can be deduced that for pulses with higher peak width the growth of electron density during peak time is more remarkable. The plots presenting the electric field and electron temperature indicate that for pulses with a big peak width the minimum electron temperature and electric field values are the smallest.

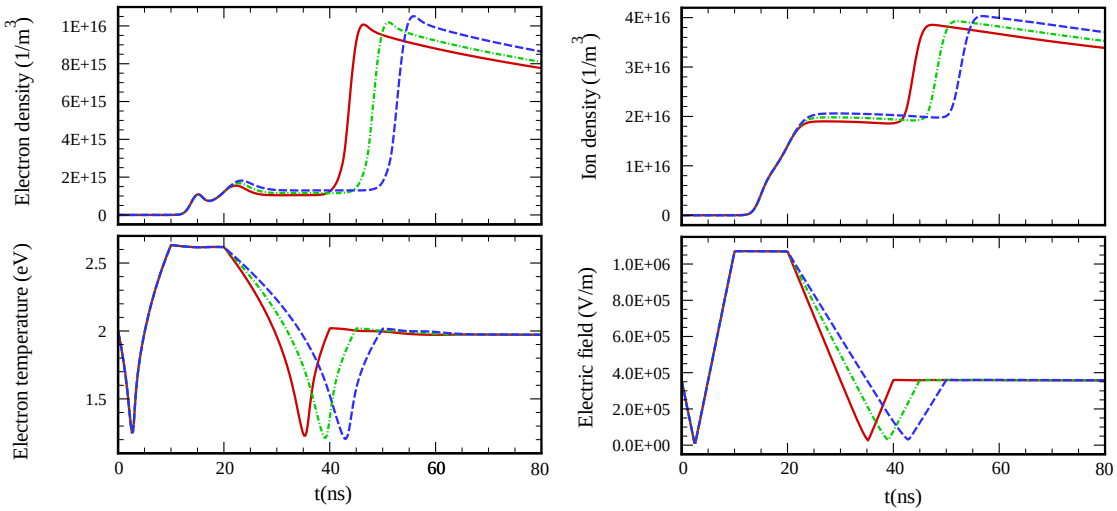

FIG. 8: Spatially averaged electron density, ion density, electron temperature, and electric field as the functions of time for three different pulse fall times 20 ns (solid), 25 ns (dash-dotted), and 30 ns (dashed).

Figure 8 illustrates the time evolution of spatiality averaged plasma parameters, same as two previous figures, for three input pulses that have different pulse fall times. As can be seen from figures, although increasing the pulse fall time increase density of plasma species (electron and ion) it is not remarkable in comparison to increase in them due to increase in the pulse rise and the pulse peak width (see figures 6 and 7). Also, magnitude of electric field and electron energy of pulses with different pulse fall times are approximately the same.

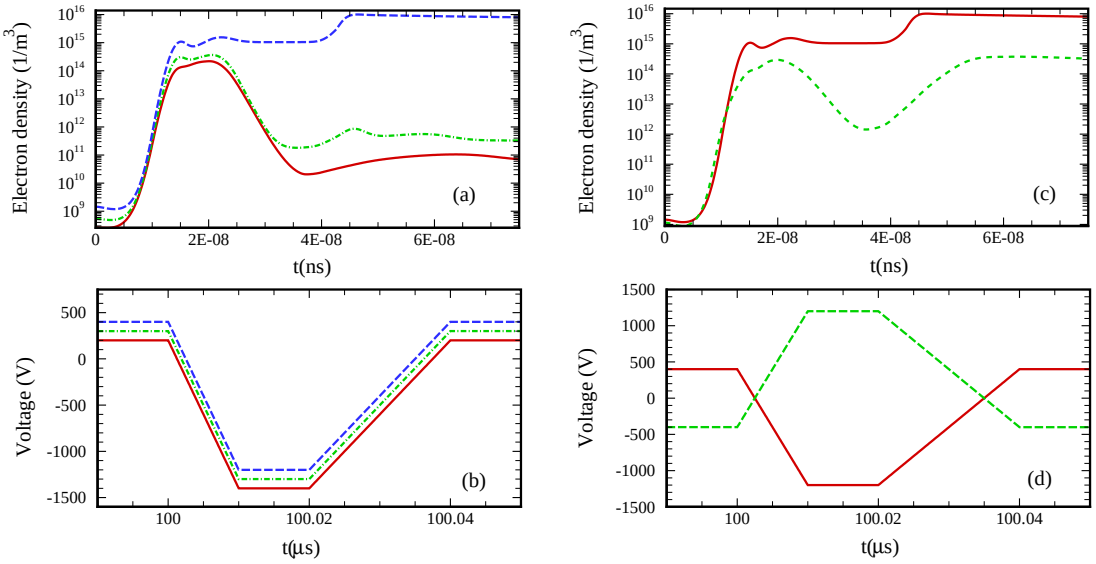

FIG. 9: Time evolution of spatially averaged electron densities for different applied voltages. The density profiles in (a) and (c) are corresponded to applied voltages (b) and (d), respectively.

Lastly, figure 9 compares the effects of different positive bias voltages and different polarities of net applied voltage (pulse+bias) on the plasma electron density. In Fig. 9(a) the time evolution of spatially averaged electron densities for three different applied voltages of Fig. 9(b) are illustrated. Voltage profiles in Fig. 9(b) are different in values of applied positive bias voltages (200 V, 300 V, 400 V) and the amplitude of negative pulse voltage is the same for all. As can be seen from Fig. 9(a), with increasing positive bias voltage not only the electron density value increases in pulse off-time but also it gets higher values in pulse on-time. Also, for higher positive bias voltages the electron density does not show a quick drop in value after pulse becomes off (after t=40 ns). This implies that how a positive bias voltage can be used to maintain the plasma being active during pulse off-time, which is important from the energy-cost aspect in plasma gas conversion applications. Figure 9(c) shows the time evolution of electron density for two applied voltages having different polarities shown in Fig. 9(d). As can be seen from the figure, when the polarity of applied voltage changes the electron density profile shows a significant change in value both during pulse off-time and during pulse on-time. For voltage profile with negative pulse voltage and positive dc bias electron density is higher than that of voltage profile with positive pulse voltage and negative dc bias and also after pulse off-time, the plasma is more active for negative pulse voltage. This is related to the secondary emission rate that is vigorous for voltages profiles having negative polarity, which was discussed in section I.

IV. CONCLUSIONS

By employing multi-species fluid model the argon plasma created in a micro dielectric barrier discharge containing charge injection points and driven by negatively polarized nanosecond pulsed voltage superimposed on a positive bias voltage was simulated. The effects of the shape of input voltage signals such as the pulse rise time, pulse peak width, and pulse fall time were investigated on plasma parameters like electron density, electron energy, ion density, and electric field. The results revealed that, during a pulse period, electron avalanche oscillates in the discharge gap between the dielectric layer and the powered electrode. The time-averaged plasma parameters upon a single pulse showed that peak for electron density and electron energy appear near the dielectric surface while maximum values of the time-averaged electric field and electron temperature emerged near the cone tip (charge injection point). Increasing pulse rise time and/or pulse peak width increased the density of electrons and ions while pulse-fall time change did not remarkably change the plasma characteristics.

The results implied that, in comparison to ac powered DBD, DBDs powered with pulsed voltage combined with low dc voltage can be a promising system to control the plasma behaviour in order to achieve high yield and high energy efficiency. The negatively pulsed voltage can prevent heat losses between pulses and improves the energy efficiency and the discharge stability without overheating effect. Also, its variables such as pulse rise and fall times, and pulse width are useful tools to adjust energy absorbtion of different reactions occurring in plasmas used in gas processing applications. The low positive dc bias can be used to maintain the plasma being active during pulse off-time. Applying negatively pulsed voltage to a electrode containing charge injection points (sharp parts) can be a effective approach to decrease the breakdown voltage and increase the self-sustainablity of plasma, due to high rate of secondary electron emission and/or field emission effects observed in length scales of a few micrometer.

V. ACKNOWLEDGEMENTS

The authors would like to acknowledge funding by the European Research Council Synergy Grant SCOPE 810182. Also, this work received financial support from the Russian Science Foundation (project 20-69-46041, Intensification of methane dry reforming on thin-film catalysts by forced periodic modulation of electric field, concentration and temperature in low temperature

plasma).

VI. DATA AVAILABILITY STATEMENT

The data that support the findings of this study are available from the corresponding author upon reasonable request.

References

[1] X.-F. Wang, Q.-Q. Fang, B. Jia, Y.-Y. Hu, Z.-C. Wang, K.-p. Yan, S.-Y. Yin, Z. Liu, and W.-Q. Tan, Scientific Reports **10**, 1 (2020).

[2] D. B. Graves, Physics of Plasmas **21**, 080901 (2014).

[3] N. De Geyter and R. Morent, Annual review of biomedical engineering **14**, 255 (2012).

[4] S. Lerouge, M. Wertheimer, and Y. L'H, Plasmas and Polymers **6**, 175 (2001).

[5] N. Jiang, C. Qiu, L. Guo, K. Shang, N. Lu, J. Li, and Y. Wu, Plasma Chemistry and Plasma Processing **39**, 227 (2019).

[6] R. Snoeckx and A. Bogaerts, Chemical Society Reviews **46**, 5805 (2017).

[7] A. Bogaerts and E. C. Neyts, ACS Energy Letters **3**, 1013 (2018).

[8] V. Fomin, P. Tretyakov, and J. Taran, Aerospace Science and Technology **8**, 411 (2004).

[9] C. Zhai, X. Chou, J. He, L. Song, Z. Zhang, T. Wen, Z. Tian, X. Chen, W. Zhang, Z. Niu, et al., Applied energy **231**, 1346 (2018).

[10] X. Cheng, L. Miao, Z. Su, H. Chen, Y. Song, X. Chen, and H. Zhang, Microsystems & nanoengineering **3**, 1 (2017).

[11] R.-C. Zhang, D. Sun, R. Zhang, W.-F. Lin, M. Macias-Montero, J. Patel, S. Askari, C. McDonald, D. Mariotti, and P. Maguire, Scientific reports **7**, 46682 (2017).

[12] S. M. Starikovskaia, Journal of Physics D: Applied Physics **39**, R265 (2006).

[13] U. Kogelschatz, Plasma chemistry and plasma processing **23**, 1 (2003).

[14] F. Massines, P. Segur, N. Gherardi, C. Khamphan, and A. Ricard, Surface and Coatings Technology **174**, 8 (2003).

[15] U. Kogelschatz, IEEE Transactions on plasma science **30**, 1400 (2002).

[16] W. S. Kang, J. M. Park, Y. Kim, and S. H. Hong, IEEE Transactions on Plasma Science **31**, 504 (2003).

[17] K. Becker, K. Schoenbach, and J. G. Eden, Journal of Physics D: Applied Physics **39**, R55 (2006).

[18] F. Iza, G. J. Kim, S. M. Lee, J. K. Lee, J. L. Walsh, Y. T. Zhang, and M. G. Kong, Plasma Processes and Polymers **5**, 322 (2008).

[19] P. J. Lindner and R. S. Besser, Chemical Engineering & Technology **35**, 1249 (2012).

[20] Y. Gao, S. Zhang, H. Sun, R. Wang, X. Tu, and T. Shao, Applied energy **226**, 534 (2018).

[21] Y. Nishida, H.-C. Chiang, T.-C. Chen, and C.-Z. Cheng, IEEE Transactions on Plasma Science **42**,

3765 (2014).

[22] O. Khalifeh, A. Mosallanejad, H. Taghvaei, M. R. Rahimpour, and A. Shariati, Applied energy **169**, 585 (2016).

[23] H. K. Song, H. Lee, J.-W. Choi, and B.-k. Na, Plasma chemistry and plasma processing **24**, 57 (2004).

[24] S. Zhang, Y. Gao, H. Sun, H. Bai, R. Wang, and T. Shao, Journal of Physics D: Applied Physics **51**, 274005 (2018).

[25] X. Wang, Y. Gao, S. Zhang, H. Sun, J. Li, and T. Shao, Applied Energy **243**, 132 (2019).

[26] S. Chen, J. Nobelen, and S. Nijdam, Plasma Sources Science and Technology **26**, 095005 (2017).

[27] A. M. Loveless, G. Meng, Q. Ying, F. Wu, K. Wang, Y. Cheng, and A. L. Garner, Scientific reports **9**, 1 (2019).

[28] A. Venkattraman and A. A. Alexeenko, Physics of plasmas **19**, 123515 (2012).

[29] D. Lee, J. M. Park, S. H. Hong, and Y. Kim, IEEE transactions on plasma science **33**, 949 (2005).

[30] S. Gadkari, X. Tu, and S. Gu, Physics of Plasmas **24**, 093510 (2017).

[31] C. De Bie, B. Verheyde, T. Martens, J. van Dijk, S. Paulussen, and A. Bogaerts, Plasma Processes and Polymers **8**, 1033 (2011).

[32] K. V. Laer and A. Bogaerts, Plasma Sources Sci. Technol **25**, 015002 (2016).

[33] X. Che, T. Shao, W. Nie, and P. Yan, Journal of Physics D: Applied Physics **45**, 145201 (2012).

[34] A. V. Likhanskii, M. N. Shneider, S. O. Macheret, and R. B. Miles, Physics of plasmas **14**, 073501 (2007).

[35] C.-C. Wang and S. Roy, Journal of applied physics **111**, 103302 (2012).

[36] Y. Liu, K. vant Veer, F. Peeters, D. Mihailova, J. Van Dijk, S. Starostin, M. Van De Sanden, and H. De Vries, Plasma Sources Science and Technology **27**, 105016 (2018).

[37] G. Hagelaar and L. Pitchford, Plasma Sources Science and Technology **14**, 722 (2005).

[38] D. F. Opaits, A. V. Likhanskii, G. Neretti, S. Zaidi, M. N. Shneider, R. B. Miles, and S. O. Macheret, Journal of Applied Physics **104**, 043304 (2008).

[39] K. Van Laer and A. Bogaerts, Plasma Sources Science and Technology **25**, 015002 (2015).

[40] A. M. Loveless and A. L. Garner, Physics of Plasmas **24**, 113522 (2017).